

Centralized control of district heating networks during failure events using discrete adjoint sensitivities

*Original*

Centralized control of district heating networks during failure events using discrete adjoint sensitivities / Pizzolato, Alberto; Sciacovelli, Adriano; Verda, Vittorio. - In: ENERGY. - ISSN 0360-5442. - (2019). [10.1016/j.energy.2017.09.102]

*Availability:*

This version is available at: 11583/2687333 since: 2017-11-14T17:40:44Z

*Publisher:*

Elsevier

*Published*

DOI:10.1016/j.energy.2017.09.102

*Terms of use:*

This article is made available under terms and conditions as specified in the corresponding bibliographic description in the repository

*Publisher copyright*

(Article begins on next page)

# Centralized control of district heating networks during failure events using discrete adjoint sensitivities

Alberto Pizzolato<sup>a,\*</sup>, Adriano Sciacovelli<sup>b</sup>, Vittorio Verda<sup>a</sup>

<sup>a</sup>*Department of Energy, Politecnico di Torino, Corso Duca degli Abruzzi 24, Turin, Italy*

<sup>b</sup>*Birmingham Center for Energy Storage (BCES), School of Chemical Engineering,  
University of Birmingham, UK*

---

## Abstract

Real-time control of district heating networks in the case of failures requires for accurate and fast strategies able to guarantee thermal comfort to all connected users. In this paper, we demonstrate a control framework that responds to these essential requirements. We minimize a global measure of discomfort based on a smooth maximum approximation. The optimization problem is solved through a gradient-based algorithm that can be naturally integrated with distributed meter readings leading to high accuracy of both forward and sensitivity analysis. Objective function gradients are computed by a discrete adjoint method, which is fast and nearly insensitive to the dimensionality of the optimization problem. The proposed framework is tested with numerical experiments on a reference medium-size distribution network in Turin. Results show that the thermal comfort of most critical users increases quickly, yielding to a nearly homogeneous discomfort distribution at the end of the optimization process. Studying the effect of the inlet pressure head on the optimized system performance reveals that a centralized operation results in increased robustness of the network and allows reducing backup pumping equipment. Furthermore, applying the proposed framework at the distribution network level yields remarkable benefits also in case of failures in the main transportation network.

*Keywords:* centralized smart control, discrete adjoint sensitivities, district heating, real-time control

---

## Nomenclature

<b>A</b>	Incidence matrix $[-]$
<b>B</b>	Fluid-dynamic resistance matrix $[\frac{1}{m \ s}]$
<b>C</b>	Conductance matrix $[\frac{W}{K}]$
$c_p$	Specific heat $[\frac{J}{kg \ K}]$

---

\*Corresponding author: alberto.pizzolato@polito.it

$D$	Pipe diameter $[m]$
$F$	Momentum source term $\left[\frac{kg}{m^2 s^2}\right]$
$\mathbf{f}$	Fluid-dynamic pseudo-load vector $\left[\frac{kg}{m s^2}\right]$
$f$	Fanning friction factor $[-]$
$f_s$	Update factor for conventional control $[-]$
$\mathbf{G}$	Mass flow rate vector $\left[\frac{kg}{s}\right]$
$g$	Gravity constant $\left[\frac{m}{s^2}\right]$
$h$	Pressure head constraint $[-]$
$\mathbf{K}$	Fluid-dynamic pseudo-stiffness matrix
$K$	Volumetric heat transfer coefficient $\left[\frac{W}{m^3 K}\right]$
$k$	Water thermal conductivity $\left[\frac{W}{m K}\right]$
$L$	Pipe length $[m]$
$\mathbf{L}_K$	Lower triangular portion of $\mathbf{K}$
$N_s$	Number of control variables $[-]$
$np$	Number of buildings $[-]$
$\mathbf{P}$	Total pressure vector $\left[\frac{kg}{m s^2}\right]$
$P$	Total pressure $\left[\frac{kg}{m s^2}\right]$
$p$	Pressure $\left[\frac{kg}{m s^2}\right]$
$p_z$	P-mean smoothness parameter $[-]$
$\mathbf{q}$	Heat load vector $[W]$
$q$	Volumetric heat generation $\left[\frac{W}{m^3}\right]$
$\mathbf{R}$	Residual vector
$\mathbf{S}$	Set of control variables
$S$	Pipe cross section $[m^2]$
$\mathbf{s}$	Control variables vector
$s$	Control variable
$S_M$	Mass source term $\left[\frac{kg}{m^3 s}\right]$
$\mathbf{T}$	Temperature vector $[K]$
$T$	Temperature $[K]$
$\mathbf{t}$	Pumping pressure head vector $\left[\frac{kg}{m s^2}\right]$
$U_{dg}$	Duct-ground global heat transfer coefficient $\left[\frac{W}{m^2 K}\right]$
$UA$	Global transmittance heat exchanger $\left[\frac{W}{K}\right]$
$\mathbf{u}$	Fluid-dynamic state variables vector
$V$	Building total volume $[m^3]$
$v$	Velocity $\left[\frac{m}{s}\right]$
$z$	Objective $[-]$
$z_h$	Height $[m]$

#### Greek symbols

$\beta$	Local friction coefficient $[-]$
---------	----------------------------------

$\gamma$	Thermal discomfort $[-]$
$\boldsymbol{\lambda}$	Adjoint variables vector
$\lambda$	Adjoint variable
$\rho$	Water density $\left[\frac{kg}{m^3}\right]$
$\Phi$	Thermal power $[W]$
$\chi$	Normalized inlet mass flow rate $[-]$
$\Xi$	Set of network branches
$\xi$	Branch
$\Psi$	Set of network nodes
$\psi$	Node

#### *Superscripts*

(0)	Design
$nb$	Number of branches
$nn$	Number of nodes

#### *Subscripts*

$b$	Building
$C$	Conventional
$ext$	External
$extr$	Extracted
$fd$	Fluid-dynamic
$fric$	Friction
$PH$	Pressure head
$sp$	Set-point
$th$	Thermal
$us$	Upstream

## 1. Introduction

The large scale utilization of locally available heat sources makes District Heating (DH) a rational and efficient domestic heating option. To date, this technology has been coupled successfully to high efficiency Combined Heat and Power (CHP) plants [1, 2], energy-intensive industries [3, 4] and renewable generation plants such as solar [5, 6], biomass [7, 8] and geothermal systems [9, 10]. Controlling district heating networks based on distributed metering systems [11] and providing high service reliability [12] are considered primary requirements for district heating integration in future energy grids. In the case of accidents, service should be restored as quickly as possible with minimal impact on the thermal comfort of customers. However, finding the optimal operation strategy for this type of systems is a time-consuming and non-trivial problem. Real-world installations often count several thermal users and generation plants that are connected through complex fluid networks. Accurate prediction of

15 the fluid-dynamic and thermal response demands for complex simulation tools. Furthermore, the large number of moving and dissipative components results in optimization problems with a high-dimensional control space.

20 Researchers dealing with planning of thermal grids mainly adopted Lumped Parameter Modeling (LPM) to predict the performance of the system. This approach reduces to the solution of (linear) mass and energy balances. If the objective function and constraints are also linear with respect to the control variables, the optimization problem can be solved by Linear Programming (LP) techniques [1] or Mixed Integer Linear Programming (MILP) [13]. However, predicting the fluid-dynamic response of fluid networks with loops, i.e. closed fluid paths, requires solving the full Navier-Stokes equations through the use of Computational Fluid Dynamics (CFD) tools. Furthermore, the non-linearity of the momentum equation yields to non-convexity of the optimization problem and requires for global-search algorithms. A popular strategy to limit computational burden of global-search algorithms is represented by reduced models for the fluid-dynamic and thermal analysis. For instance, Jamieson et al. [14] minimized pumping cost using a Genetic Algorithm (GA) and Artificial Neural Network (ANN) to compute the fitness function. Shamir et al. [15] used GA coupled to a reduction technique called skeletonization, which allowed reducing the Water Distribution Network (WDN) network representation from 867 to 77 nodes. Guelpa et al. [16] used GA and Proper Orthogonal Decomposition (POD) to find the optimal pumping strategy in a District Heating Network (DHN). Following a parallel research direction, some authors adopted meta-heuristic techniques with improved convergence rate that allowed retaining full complexity of the network model. Most often, this is achieved by coupling heuristic and deterministic algorithms. 40 Liberatore [17] used a Scatter Search (SS) technique coupled to the pressure reference method to reduce the size of the population required by GA. The authors of [18] limited the GA search space to a few integer design variables (e.g. isolation valves) and used LP to obtain the optimal setting of the control valves. Giacomello et al. [19] also developed a hybrid algorithm for pump scheduling by combining a Greedy algorithm with LP. Also purely heuristic algorithms with fast convergence proliferated in the WDN community. Examples include Ant Colony Optimization (ACO) ([20]), Limited Discrepancy Search (LDS) [21], Particle Swarm Optimization (PSO) [22] and Harmony Search (HS) [23].

50 These important contributions result in moderate or high computational complexity. For this reason, they can hardly be utilized for real-time network control during failures, where computational time is a primary constraint [24]. Furthermore, using population-based optimization algorithms for intelligent control based on metered data shows limitations. Control actions can be started only *at the end* of the optimization and no feedback from the measuring devices can be easily integrated in the optimization procedure. Gradient-based algorithms based on adjoint sensitivities have the potential to solve both issues. At the cost of local convergence, these methods lead to faster convergence compared to enumeration or meta-heuristic techniques especially when the system analysis is particularly costly, such the solution of a CFD model. Objective 60 gradients in problems with many control variables and few constraints can be

obtained cheaply through adjoint calculus. As we discussed in a previous work [25], these features makes it a recommended choice to regulate dissipative components in large systems. Moreover, a feedback from meter readings can be easily integrated on-the-fly. The numerical model can be calibrated to measured data at each optimization iteration (after a valve update) increasing the accuracy of both the forward and the sensitivity analysis. With this approach, control actions can be taken *during* the optimization process. Figure 1(a) shows a schematic of a possible gradient-based control system, which integrates feedbacks from metered data. For comparison, Figure 1(b) shows a feed-forward control strategy using a population-based algorithm. This work aims at providing a thorough proof-of-concept on the use of a centralized control with adjoint sensitivities to handle DHNs failures. Control is operated following a global measure of maximum thermal discomfort, which ensures differentiability. At each optimization iteration, the fluid-dynamic and thermal responses are computed through a 1D CFD model based on a graph representation of the network. To test the proposed framework we consider the Turin DHN, which is the largest installation in Italy [26].

The remainder of this paper is organized as follows. Section 2 presents the numerical model used to predict the fluid-dynamic and thermal response of the network. Section 3 discusses the optimization problem formulation along with a complete description of the sensitivities calculation step. Section 4 reports the most relevant numerical details. Section 5 presents and discusses the results obtained. Finally, a summary and some concluding remarks are presented in Section 6.

## 2. Physical model of the network

This section presents the governing equations and the discretization strategy used to predict the thermal and fluid-dynamic response of the network. We use a 1D finite volume model [16, 26] to calculate the mass flow rate vector  $\mathbf{G}$ , the total pressure vector  $\mathbf{P}$  and the temperature vector  $\mathbf{T}$ .

A schematic of the modeling framework is given in Figure 2. The network is represented through a graph approach [27] where each pipe is considered as a branch (indicated with a black solid line) delimited by two nodes (indicated with black solid circles), which physically correspond to either bifurcations or conjunctions. Hot water is injected in the system at the inlet node, located at the outlet cross section of the power plant pumping system. Please note that the thermal response of the buildings is also calculated in the present framework. We include a set of user branches (indicated in green) that are considered as separate entities, where we model the building-system interaction through the building heat exchanger. The degrees of freedom corresponding to the mass flow rates are defined at each branch while those corresponding to temperatures and pressures are defined at each node in a staggered grid fashion. The network topology is uniquely represented by the incidence matrix  $\mathbf{A} : \mathbb{R}^{nb} \rightarrow \mathbb{R}^{nn}$ , where  $nb$  is the number of branches and  $nn$  is the number of nodes. Let  $\mathbf{N}$  be the graph

representation of the network with branches  $\Xi(\mathbf{N}) = \{\xi_1, \xi_2, \dots, \xi_{nb}\}$  and nodes  
105  $\Psi(\mathbf{N}) = \{\psi_1, \psi_2, \dots, \psi_{nn}\}$ . The incidence matrix  $\mathbf{A}$  is defined such that:

$$A_{ij} = \begin{cases} +1 & \text{if } \psi_i \text{ is the inlet node of branch } \xi_j \\ -1 & \text{if } \psi_i \text{ is the outlet node of branch } \xi_j \\ 0 & \text{otherwise} \end{cases} \quad (1)$$

We assume a steady-state and incompressible flow with constant fluid properties and negligible viscous dissipation. The 1D continuity equation is readily written as:

$$\rho \frac{\partial v_1}{\partial x_1} = S_M \quad (2)$$

where  $\rho$  is the water density,  $v_1$  is the water velocity along the pipe axis and  
110  $S_M$  is a mass source term. After integration over the nodal control volume (indicated in red in Figure 2), Eq. (2) can be casted in the following discrete form:

$$\mathbf{A}\mathbf{G} + \mathbf{G}_{extr} = 0 \quad (3)$$

where  $\mathbf{G}_{extr}$  is a nodal mass flow rate extraction vector. The steady-state incompressible 1D momentum equation is written as:

$$\rho v_1 \frac{\partial v_1}{\partial x_1} = -\frac{\partial p}{\partial x_1} - F_{fric} + F_{pump} + \rho g_1 \quad (4)$$

115 where  $p$  is the pressure,  $F_{fric}$  accounts for viscous effects,  $F_{pump}$  is a momentum source term due to the presence of pumps and  $g_1$  is the projection of the gravity vector on the pipe axis. Integration of (4) over the branch control volume (indicated in blue in Figure 2) leads to:

$$(P_{out} - P_{in}) = -\Delta P_{fric} + \Delta P_{pump} \quad (5)$$

where  $P$  is the total pressure defined as:

$$P = p + \rho \frac{v^2}{2} + \rho g z_h \quad (6)$$

120 where  $g$  is the gravity constant and  $z_h$  the height. The first term on the right-hand side of Eq. (5) is written considering semi-empirical correlations of the form:

$$\Delta P_{fric} = \frac{1}{2} \rho v_1^2 \left( f \frac{L}{D} + \sum_k \beta_k \right) \quad (7)$$

where  $f$  is the Fanning friction factor,  $\beta_k$  is the local friction coefficient of the  
125  $k^{th}$  friction source,  $D$  is the pipe diameter and  $L$  is the pipe length. Eqs. (5) through (7) can be rearranged to obtain the following non-linear system:

$$\mathbf{B}\mathbf{G} - \mathbf{A}^T \mathbf{P} - \mathbf{t} = \mathbf{0} \quad (8)$$

where  $\mathbf{B}$  is a diagonal non-linear operator which contains the fluid-dynamic resistance of each branch in the network as following:

$$B_{jj}(G_j) = \frac{G_j \left( \frac{f}{D_j} L_j + \sum_k \beta_{k_j} \right)}{2\rho S_j^2} \quad (9)$$

where  $S_j$  is the pipe cross section. The column vector  $\mathbf{t}$  contains the pumping pressure heads  $\Delta P_{pump_j}$  applied in each branch of the network. The vector of  
130 fluid-dynamic residuals can be written in a unique coupled system as following:

$$\mathbf{R}_{fd} = \mathbf{K}\mathbf{u} - \mathbf{f} = \mathbf{0} \quad (10)$$

where the non-linear operator  $\mathbf{K}$  is defined as:

$$\mathbf{K} = \begin{bmatrix} \mathbf{A} & \mathbf{0} \\ \mathbf{B} & -\mathbf{A}^T \end{bmatrix} \quad (11)$$

the total state variable vector  $\mathbf{u}$  is defined as:

$$\mathbf{u} = \begin{Bmatrix} \mathbf{G} \\ \mathbf{P} \end{Bmatrix} \quad (12)$$

and the vector  $\mathbf{f}$  is defined as:

$$\mathbf{f} = \begin{Bmatrix} -\mathbf{G}_{ext} \\ \mathbf{t} \end{Bmatrix} \quad (13)$$

135 To calculate the thermal response, we consider the steady-state version of the 1D convection-diffusion equation. The steady-state assumption implies that the control actions last longer than the characteristic time of the network and that no variation of the thermal demand is registered. This choice is motivated by the enhanced modeling simplicity, which is desirable in this demonstrative paper.  
140 Under the modeling assumptions, the energy equation can be written as:

$$\rho c_p v_1 \frac{\partial T}{\partial x_1} = k \frac{\partial^2 T}{\partial x_1^2} + q \quad (14)$$

where  $c_p$  is the water specific heat,  $k$  is the water thermal conductivity and  $q$  is a volumetric heat generation term. The first term on the right-hand side is neglected since the convective term is dominant. Integrating over a nodal control volume (indicated in red in Figure 2) we obtain:

$$\rho c_p \sum_{j=1}^{N_{b_i}} v_{1_j} T_j S_j = \frac{1}{2} \sum_{j=1}^{N_{b_i}} L_j \pi D_j U_{dg} (T_i - T_{ext}) \quad (15)$$

145 where  $N_{b_i}$  is the number of branches connected to node  $i$ ,  $U_{dg}$  is the global heat transfer coefficient of the duct-ground system and  $T_{ext}$  is the external



temperature. Eq. (15) can be casted in matrix form to obtain the following linear system:

$$\mathbf{R}_{th} = \mathbf{C}\mathbf{T} - \mathbf{q} = \mathbf{0} \quad (16)$$

where  $\mathbf{C}$  is the conductance matrix assembled using the upwind scheme [28] for the advective term of Eq. (15),  $\mathbf{T}$  is the nodal temperature vector and  $\mathbf{q}$  is the heat load vector which collects all the constant terms of the heat losses. Special care should be taken at the user nodes when assembling the system of Eq. (16). Let us consider a generic building  $i$  for which we write an integral energy balance as:

$$G_j c_p (T_{i,in} - T_{i,out}) = K V_i (T_{i,b} - T_{ext}) \quad (17)$$

where  $G_j$  inlet mass flow rate at the building heat exchanger,  $T_{i,in}$  and  $T_{i,out}$  are the water inlet and outlet temperatures of the heat exchanger,  $V_i$  is the building volume,  $K$  is the volumetric heat loss coefficient and  $T_{i,b}$  is the building temperature. This equation can be solved considering the thermal balance across the heat exchanger to calculate the outlet temperature  $T_{i,out}$ , i.e.:

$$G_j c_p (T_{i,in} - T_{i,out}) = (UA)_i \left( \frac{T_{i,in} + T_{i,out}}{2} - T_{i,b} \right) \quad (18)$$

where  $(UA)_i$  is the global transmittance of the heat exchanger obtained through experimental data, which includes both the heat exchanger and the building heat delivery system efficiencies. Note that to we have linearized the characteristic temperature difference driving heat transfer across the heat exchanger.

To solve the fluid-dynamic model, we prescribe the total pressure  $P_{out}$  at the outlet of the network and the mass flow rate  $G_{in}$  at the inlet. Mathematically:

$$P_i = P_{out} \quad \text{if } \psi_i \in \Gamma_2 \quad (19)$$

$$\mathbf{G}_j \cdot \mathbf{n} = G_{in} \quad \text{if } \psi_i \in \Gamma_1 \quad (20)$$

where  $\mathbf{n}$  is the inward-pointing normal depicted in Figure 2. To solve the thermal model, we prescribe the inlet water temperature  $T_{in}$  as following:

$$T_i = T_{in} \quad \text{if } \psi_i \in \Gamma_1 \quad (21)$$

The utilization of thermal balance on the user branch (Eq. (17)) does not require the imposition of an additional outflow boundary condition.

### 3. Optimization problem formulation

In this section we discuss the optimization problem formulation including the control variables, the objective, the constraints and the sensitivities calculation. Furthermore, we describe a way to mimic the control strategy in use today.

### 175 3.1. Control variables

After a pipe breakage event, the interested pipe gets isolated from the network. This action moves the fluid-dynamic equilibrium to a point which is far from being optimal. The thermal demand of the users located in remote areas of the network, i.e. with a low available pressure head, will hardly be satisfied. 180 A centralized management strategy should avoid this situation by controlling the user control valves. Hence, the vector of control variables  $\mathbf{s}$  is used to interpolate linearly the local pressure drop coefficient of the user control valves as following:

$$\beta_j(s_j) = \beta_{min} + (\beta_{max} - \beta_{min})s_j \quad j = \{1, \dots, N_s - 1\} \quad (22)$$

where  $\beta_{min}$  and  $\beta_{max}$  are the minimum and maximum local pressure drop coefficients and  $N_s$  is the number of control variables. Since the equivalent fluid-dynamic resistance is changed by the control, the inlet mass flow rate  $G_{in}$  should also be allowed to vary in order to satisfy a maximum available pressure head constraint. Hence we also have:

$$G_{in}(s_{N_s}) = G_{in}^{(0)}(\chi_{max} - \chi_{min})s_{N_s} \quad (23)$$

where  $\chi_{min}$  and  $\chi_{max}$  are the minimum and maximum mass flow rates normalized to the design value of  $G_{in}^{(0)}$ . 190

### 3.2. Objective and constraints

Our centralized control strategy aims at minimizing the maximum thermal discomfort of the buildings connected. We name this control strategy as Least Maximum Discomfort, hereafter referred as LMD-Control. The thermal discomfort  $\gamma_j$  of the building  $j$  is written as: 195

$$\gamma_j = \left( \frac{\Phi_j - \Phi_{spj}}{\Phi_{spj}} \right)^2 \quad (24)$$

where  $\Phi_j$  is thermal power transferred from the network to the building while  $\Phi_{spj}$  is the ideal thermal power that would be required to obtain the internal setpoint temperature  $T_{sp}$ . Mathematically:

$$\Phi_{spj} = KV_j(T_{sp} - T_{ext}) \quad (25)$$

where  $V_j$  is the total volume of the building,  $K$  is the volumetric heat transfer coefficient and  $T_{ext}$  is the external temperature. The term in brackets of (24) has a clear physical significance: it represents the thermal power deficit or surplus in relative terms. We will refer to this quantity as thermal mismatch  $\|\Delta\Phi\|$  hereafter. The quadratic formulation presented in Eq. (24) allows to equally account for buildings over-heated and buildings under-heated. To obtain the fluid-dynamic equilibrium of the system we should prescribe the intersection 205 between the network and the pump characteristic curves. The latter is here

assumed as constant. The optimization problem is thus augmented by a pressure head constraint of the form:

$$h(\mathbf{u}(\mathbf{s}), \mathbf{s}) = (\Delta P_{PH} - \Delta P_{max})^2 - \epsilon^2 \leq 0 \quad (26)$$

Eq. (26) is imposed weakly such that in the worst case the maximum pressure drop registered in the network  $\Delta P_{max} = \max(\mathbf{P}) - \min(\mathbf{P})$  differs from the pressure head  $\Delta P_{PH}$  by a small number  $\epsilon = 1e-4$ . To sum up, the optimization problem is formulated as:

$$\begin{aligned} \min_{\mathbf{s}} \quad & z = \left( \frac{1}{np} \sum_{j=1}^{np} \gamma_j^{p_z} \right)^{\frac{1}{p_z}} \\ \text{s.t.} \quad & h(\mathbf{u}(\mathbf{s}), \mathbf{s}) \leq 0 \\ & \mathbf{s} \in \mathbf{S} = \{\mathbb{R}^{N_s} \mid s_{min} < s_i < s_{max}, i = 1, \dots, N_s\} \end{aligned} \quad (27)$$

where  $np$  is the number of buildings connected to the network, and  $p_z$  is a parameter that control the smoothness with which the maximum function is approximated. The p-mean formulation presented in (27) provides a lower bound to the hard maximum function and converges to it in the limit of [29]:

$$\lim_{p_z \rightarrow \infty} z = \max(\gamma_j) \quad (28)$$

This approach ensures differentiability and stabilizes convergence if large  $p_z$  values are avoided. The box constraint sets a lower bound  $s_{min} = 0$  and an upper bound  $s_{max} = 1$  to each control variable  $s_i$  in the  $N^s$ -dimensional control space. We adopt the nested analysis and design approach, where the state variables are implicitly dependent on the control variables through the state equations. For this reason, we do not include the state equations in the set of equality constraints of (27), but we calculate the fluid-dynamic and thermal response at each iteration of the optimization process. Problem (27) in general does not satisfy standard constraint qualifications. Linear Independence Constraint Qualification (LICQ) is checked a-posteriori on the candidate solution. Furthermore, we cross-checked the results obtained considering a similar non-linear program to (27) without the pressure head constraint, which is satisfied implicitly during the analysis by imposing an inlet pressure boundary condition. It is easy to show that this modified problem satisfies the LICQ. Also note that all the components of the gradient of the pressure head constraint in (27) is non-zero. Hence, if one or more design variables *strictly* satisfies the box constraint, LICQ holds.

### 3.3. Sensitivities calculation

The derivatives of the objective and constraints with respect to the control variables are needed by a gradient-based optimization method. The adjoint approach is particularly convenient for optimization problems with a large number of control variables and few constraints, since it requires solving one additional

linear problem per objective and constraint. The discrete sensitivities field is  
240 calculated as:

$$\frac{dz}{ds} = -\lambda_{fd}^T \frac{\partial \mathbf{R}_{fd}}{\partial \mathbf{s}} - \lambda_{th}^T \frac{\partial \mathbf{R}_{th}}{\partial \mathbf{s}} \quad (29)$$

where  $\lambda_{fd}$  is the vector of adjoint variables of the fluid-dynamic problem and  $\lambda_{th}$  is the vector of adjoint variables of the thermal problem. The partial derivatives appearing in (29) are written considering the double nature of the control variables. The first  $N_s - 1$  act on the fluid-dynamic resistance of the user branch  
245 while the last one modifies the inlet mass flow rate. Recalling Eqs. (9), (20), (21) and (22), we obtain:

$$\left( \frac{\partial \mathbf{R}_{fd}}{\partial \mathbf{s}} \right)_{i,j} = \begin{cases} (\beta_{max} - \beta_{min}) \frac{G_j^2}{2pS_j^2} & \xi_i \text{ is a user branch controlled by } s_j \\ -1 & \text{if } \psi_i \in \Gamma_1, j = N_s \\ 0 & \text{otherwise} \end{cases} \quad (30)$$

and

$$\left( \frac{\partial \mathbf{R}_{th}}{\partial \mathbf{s}} \right)_{i,j} = \begin{cases} c_p T_0 & \text{if } \psi_i \in \Gamma_1, j = N_s \\ 0 & \text{otherwise} \end{cases} \quad (31)$$

The adjoint variables are calculated solving consecutively two discrete adjoint problems of the form:

$$\left( \frac{\partial \mathbf{R}_{th}}{\partial \mathbf{T}} \right)^T \lambda_{th} = \frac{\partial z}{\partial \mathbf{T}} \quad (32)$$

250

$$\left( \frac{\partial \mathbf{R}_{fd}}{\partial \mathbf{u}} \right)^T \lambda_{fd} = -\lambda_{th}^T \frac{\partial \mathbf{R}_{th}}{\partial \mathbf{u}} \quad (33)$$

where the term on the left-hand side of Eq. (32) is readily obtainable since we are dealing with a linear system:

$$\frac{\partial \mathbf{R}_{th}}{\partial \mathbf{T}} = \mathbf{C} \quad (34)$$

and the right-hand side is calculated as:

$$\left( \frac{\partial z}{\partial \mathbf{T}} \right)_i = \frac{2\gamma_i^{p_z}}{np(T_i - T_{sp})} \left( \frac{1}{np} \sum_{j=1}^{np} \gamma_j^{p_z} \right)^{\left( \frac{1}{p_z} - 1 \right)} \quad (35)$$

Moving to the left-hand side of Eq. (33) we have:

$$\frac{\partial \mathbf{R}}{\partial \mathbf{u}} = \mathbf{K} + \mathbf{L}_K \quad (36)$$

255 where  $\mathbf{L}_K$  is the stricly lower triangular portion of  $\mathbf{K}$  in block form (Eq. (11)) that includes only  $\mathbf{B}$ . The right-hand side of (33) reads:

$$\left( \frac{\partial \mathbf{R}_{th}}{\partial \mathbf{u}} \right)_{i,j} = \begin{cases} c_p T_i & \text{if } \psi_i \text{ is the inlet node of } \xi_j \\ -c_p T_{us} & \text{if } \psi_i \text{ is the outlet node of } \xi_j \\ 0 & \text{otherwise} \end{cases} \quad (37)$$

where  $T_{us}$  is the temperature of the upstream node according to an upwind discretization procedure for the advective term. Note that the one-way coupling characteristic of forced convection is reversed for the computation of the adjoint variables, i.e. the adjoint temperature field introduces a forcing term in the adjoint total pressure and mass flow rate field. A similar procedure is followed to calculate the sensitivities of the pressure head inequality constraint (Eq. (26)).

### 3.4. Conventional Control

In order to allow for useful comparisons, we reproduce a control strategy to handle branch failures, which we call conventional control and label as C-Control in the subsequent treatment. Nowadays, most of the district heating networks do not have a centralized control on single buildings and decisions are taken from each individual user based on their local degree of discomfort. In other words, users that are over-heated close their control valve while buildings under-heated open it. However, there is an intrinsic hierarchy in the control possibility. While the control action of the former ones is always successful (a valve can always be *closed more*), the degree of discomfort of the latter ones is dictated by fluid-dynamic constraints. In fact, even if the valve is completely open, the incoming mass flow rate can still be non-sufficient if the pressure head is below the required value. This double nature of the control leads to model the behavior of the two user types separately. The over-heated buildings are handled by using the optimization problem described in Eq. (27) with a slight modification to the objective function:

$$z_C = \left( \frac{1}{\bar{n}p} \sum_{k=1}^{\bar{n}p} \gamma_j^{p_z} \right)^{\frac{1}{p_z}} \quad (38)$$

where  $\bar{n}p$  is the total number of buildings in which:

$$\Phi_k - \Phi_{sp_k} > 0 \quad (39)$$

For the under-heated buildings, we adopt a heuristic recursive relation of the form:

$$s_l^{(i+1)} = s_l^{(i)} - f_s s_l^{(0)} \quad (40)$$

where  $s_l^{(0)}$  is the design control variable value while  $s_l^{(i)}$  is its value at the optimization iteration  $i$  and  $f_s$  is a constant scalar factor here set to 0.2. Here  $l$  runs over those buildings in which:

$$\Phi_l - \Phi_{sp_l} < 0 \quad (41)$$

No control action is taken for those buildings where  $\Phi = \Phi_{sp}$ . This heuristic procedure adds on the deterministic update given by the optimizer and yields significant modifications to the optimization routine only in the first iterations.

#### 4. Numerical implementation

290 The fluid-dynamic problem of Eq. (10) is solved through the SIMPLE algo-  
rithm of Patankar et al. [30] and an under-relaxed fixed-point iteration method  
to deal with the non-linearity of the momentum equation. Numerical experi-  
ments have shown that setting the under-relaxation parameter to 0.8 yields an  
acceptable trade-off between stability and computational cost. Outer iterations  
295 are stopped when  $L_2$  norm of the relative residuals drops below  $1e - 9$ . The  
linear systems arising at each fixed-point iteration, at each SIMPLE iteration  
and in the sensitivity analysis are solved through a direct method in Matlab.  
The optimization problems are solved using the Method of Moving Asymptotes  
(MMA) of Svanberg et al. [31]. The general idea behind the MMA is to solve a  
300 series of convex and separable subproblems obtained by a first order approxima-  
tion of the original problem. Those approximation are obtained by linearization  
in pseudo-reciprocal variables of the type  $1/(s_i - L_i)$  or  $1/(U_i - s_i)$  depending on  
the sign of the sensitivity. The parameters  $U_i$  and  $L_i$  are denominated upper and  
lower moving asymptotes. To ensure feasibility, some elastic variables are in-  
305 troduced in the problem. In the present framework, the subproblems are solved  
with an interior-point primal-dual method. The major advantage of MMA, is  
the ability of dynamically controlling the asymptotes during the optimization.  
This both stabilizes and accelerates convergence making it an ideal approach to  
optimize systems requiring really expensive analysis and/or fast convergence.  
310 The relevant MMA parameters are provided in Table 1. The constraint penalty  
multiplies an elastic variables term appearing in the objective. We choose a  
rather large value to obtain as much as possible a sequence of feasible solutions  
of the original problem. Larger values are not recommended to avoid numerical  
difficulties [31]. Convergence is considered satisfactory when the relative change  
315 in the objective is less than  $1e - 5$  for 5 consecutive iterations and all constraints  
are satisfied. The  $p_z$  value chosen for the p-mean formulation presented in (27)  
is set to 8 in this paper. Wiggling in the objective history was observed for  
larger values due to ill-scaled sensitivities. On the other hand, lower values  
result in a worse approximation of the hard maximum function. The presented  
320 modeling framework has been validated with experimental results obtained from  
the Turin district heating network, see for instance [16, 26]. The accuracy of  
the sensitivities calculation step has been checked against finite differences in  
preliminary numerical studies.

#### 5. Results and discussion

325 This section presents the numerical studies and discusses the results ob-  
tained. The Turin DHN counts around 5500 buildings connected for a total  
thermal request of 1.3 GW in design conditions. The system is composed of  
a transportation and a distribution network. The transportation network con-  
nects the thermal plants to each distribution network, which in turn supplies  
330 water to users located in the vicinity of the connecting node.

To test the effectiveness of the proposed approach we focus on the control of a medium-size distribution network that delivers thermal energy to 110 buildings. A representation is given in Figure 3. This subnetwork consists of 231 branches and is designed to satisfy a total thermal request of 17.6 MW. It is connected to the main transportation network in two points, which are labeled as 'Inlet 1' and 'Inlet 2' in Figure 3. 'Inlet 2' is usually closed and can be opened in the case of abnormal operating conditions (e.g. failure in a branch). The values of the most relevant parameters and properties are summarized in Table 2. We simulate a failure by isolating the failed branch resulting in a modified topology of the network. We consider looping branches, i.e. those pipes that do not prevent any user from being reached by hot water. In the remainder of this section, we first shed light on the LMD-Control procedure focusing on a reference case with a failure in branch 16 (Figure 3), which is the one showing the largest effect on the system performance. Then, we assess the effect of the available pressure head for different failed branches and inlet positions. Last, we study how failures in the main transport network can be handled through a centralized control of the considered distribution network.

### 5.1. Using the LMD-Control to handle failures

In this section we minimize our discomfort measure considering a failure in branch 16. Water is injected in the network through 'Inlet 1', as indicated in Figure 3. The objective history for the first 100 iterations during the optimization is shown in Figure 4. Note that Figure 4 does not show the whole optimization history. Convergence according to the termination criterion specified in Section 4 is reached after 134 iterations. The objective history is smooth and improvements are quick. The maximum discomfort measure drops by more than 60 % in the first 20 iterations while it takes 80 more iterations to obtain an additional 20 % reduction. The initial discomfort field peaks in the region located right downstream the malfunction. The thermal mismatch of this group of users is rapidly increased by redirecting some of the thermal power of their neighbors. This smoothing process progressively enlarges the area with negative thermal mismatch, which reaches the northern part of the network after 20 iterations. At this point, it is still possible to clearly distinguish among three different zones: a cold zone (blue), an intermediate zone (green) and a warm zone (orange). The former two appear mixed together after 50 iterations and a nearly homogeneous thermal mismatch field is observable after 100 iterations.

Figure 5 shows a comparison of the final thermal mismatch distribution obtained with the two control strategies. The LMD-Control allows obtaining a nearly flat thermal mismatch field. On the other hand, the conventional operation strategy results in strong discomfort peaks. Users located right downstream the broken pipe feel the highest thermal discomfort. Thermal power flows according to the head availability at the user. If the available head is below the design value even when the control valve is completely open, the setpoint power cannot be guaranteed. It is easy to localize the region in which the available pressure head drops below the required value. The thermal mismatch field is

375 nearly completely homogeneous except for the south-east region of the network where the user temperature gradually drops.

These results demonstrate the effectiveness of our control strategy in handling branch failures. Thermal mismatches are quickly balanced avoiding discomfort peaks that naturally arise when using the conventional control strategy.

## 380 5.2. The effect of available pressure head

Here we investigate how the available pressure head at the inlet of the distribution network affects the capabilities of our control strategy. We systematically relax the pressure head constraint of Eq. (27):  $\Delta P_{PH}$  is increased in 6 steps of 14 % over the design value. For each value, an optimization run is performed. 385 Similarly to the previous section, we consider a failure in branch 16 and water is injected through 'Inlet 1'.

The obtained trends for the LMD-Control and the C-Control are reported in Figure 6. These values correspond to the objective defined in (27) normalized with respect to the initial objective of the case with no additional pressure head. 390 Increasing the available pressure head has moderate effect on the performance of our centralized control strategy. It is possible to decrease the normalized objective from 18.0 % to 0.2 % with an 84 % increase of the pressure head. On the other hand, Figure 6(b) indicates that an increase of the inlet pressure head is crucial for the correct handling of failures when using the conventional operation strategy. The maximum discomfort obtained with the LMD-Control and no additional pressure head is 45 % lower than the one obtained with the C-Control and 84 % additional pressure head. This suggests that our control strategy is a valid alternative to a backup pumping system at the inlet of the distribution network. Figure 7(a) shows the optimized mass flow rate versus 400 the pressure head increase over the nominal value. The ordinate values are normalized with respect to a design mass flow rate of 89.16 kg/s. Both control strategies result in a reduced value compared to the design one. The reduction required when using the LMD-Control case is lower than when using the C-Control. If the users in the vicinity of the inlet tolerate a positive  $\|\Delta\Phi\|$  then 405 the equivalent network fluid-dynamic resistance diminishes and the pump can elaborate more mass flow rate. This is visible in Figure 7(b), which shows the thermal mismatch range, defined as  $(\max \|\Delta\Phi\| - \min \|\Delta\Phi\|)$ . With no additional pressure head, the thermal mismatch obtainable with the LMD-Control ranges from a minimum of -13.8 % to a maximum of 6.7 %. As we raise the network pressure head this gap decreases in a linear fashion to reach a difference of only 0.1 % with the maximum pressure head considered. The C-Control shows serious limitations in handling the low pressure head cases. In this case, the minimum thermal mismatch registered is -70.3 % for the lowest pressure head case. With additional pumping power in the system, this value scales as 410  $\min \|\Delta\Phi\| \sim -\Delta P_{PH}^2$  and reaches a maximum of -19.0 %.

Figure 8 shows the evolution of the thermal mismatch distribution for three different values of pressure head increase. The snapshots are taken after 20, 50 and 100 iterations. Similar improvements are achieved with the first 20 iterations: the thermal mismatch peaks are *spread* and *flattened* to the whole



420 south-east region of the network in all the cases considered. From the 20<sup>th</sup> to the 50<sup>th</sup> iteration, the cold wave expands to occupy the whole southern portion, while the northern portions look still warm. Substantial differences among the three cases are visible after the 50<sup>th</sup> iteration. In this phase, the over-heated buildings contribute meaningfully to the objective and the optimizer tries to  
 425 meld the hot and the cold region in unique homogeneous field. The success of this last step largely depends upon the value of additional pressure head: with 0 % and 42 % additional pressure head, a hotspot is visible in the region close to the inlet. With 84 % additional pressure head, the LMD-Control nearly restores the original temperature field prior to failure.

430 This section shows that a centralized operation strategy is less sensitive to branch failures and pressure head variations resulting in increased robustness of the network. Furthermore, results suggest that the LMD-Control can handle failures without requiring an increased pressure head and possibly yields investment savings on backup pumping equipment at the inlet of the distribution  
 435 network.

### 5.3. The effect of network topology and inlet position

In this section, we first investigate how the effectiveness of the proposed control framework is affected by network topology, which we modify by simulating failures in other branches. Then we study the effect of the position of  
 440 the network inlet. The numerical experiments presented in the previous section are repeated considering failures in branch 72 and 143 and an alternative inlet position, indicated in Figure 3 as 'Inlet 2'.

Figure 9(a) shows the final normalized objective for different values of pressure head when handling a failure in branch 143 and branch 72. The trend for  
 445 branch 16, which was already presented in Figure 6, is also reported to facilitate comparisons. To obtain these results, the inlet position has been set according to the reference configuration, i.e. 'Inlet 1'. The three curves drop at different rates. This indicates that the network topology influences the effect of available pressure head on discomfort peaks. With no additional pressure head, a failure  
 450 in branch 16 yields the highest objective value. However, this case has the lowest objective when the pumping power is increased by 84 % over the design value. Figure 9(b) summarizes the increase of the minimum thermal mismatch obtained with the LMD-Control compared to the C-Control. In all the cases considered the performance gap between control strategies drops quadratically  
 455 when the pressure head is increased.

The final normalized objective for the two different inlet positions is shown in Figure 10. Note that here we consider a failure in branch 16 in agreement with the reference configuration. The two curves exhibit a nearly constant spacing along the y axis and drop at the same rate. This suggests that the inlet position  
 460 does not influence the effect of available pressure head on discomfort peaks. The improvements obtained with the LMD-Control compared to the C-Control are summarized in Figure 10. With no additional pressure head, gains are higher with 'Inlet 1' compared to 'Inlet 2'. Raising the pressure head results in a quadratic and linear trend for 'Inlet 1' and 'Inlet 2' respectively. As a result,

465 with an 84 % additional pressure head the LMD-Control yields larger benefits when water is injected in 'Inlet 2'.

The results presented in this section indicate that, when using the LMD-Control, the effect of available pressure head on the thermal discomfort is affected by the network topology but not by the inlet position. However, different  
470 conclusions are drawn when considering how improvements with respect to the C-Control vary with the available pressure head. Those are found to be mainly affected by the inlet position and only minor differences are due to the network topology.

#### 5.4. Failure in the transportation network

475 In this numerical study, we investigate the performance of the proposed control strategy during a failure in the main supply line (transportation network) of the Turin district heating network, depicted in Figure 11(a). The graph representation of this system counts 1373 nodes and 1389 branches. Hot water is injected in six different positions highlighted with green indicators. Those  
480 correspond to the location of CHP plants, boilers and storage tanks. We consider two malfunctions, hereafter referred as 'Failure 1' and 'Failure 2'. In both cases, the location of the most critical distribution network, i.e. the one with the lowest available pressure head, corresponds to the one indicated in Figure 11(a). For simplicity, we assume that this critical subnetwork has the same  
485 topology (without any failure) and design specifications of the one considered in the previous sections. Water is injected in this distribution network through 'Inlet 1', as in the reference case.

To properly account for the network-subnetwork interaction, a constant available pressure head at the inlet section of the subnetwork cannot be considered. Fluid-dynamic equilibrium is given by the intersection between the  
490 characteristic pressure curves of the two systems. The main network characteristic curves during the two failures alongside with the subnetwork control curves for both LMD-Control and C-Control are reported in Figure 11(b). All values are normalized with respect to the nominal operating condition. The  
495 subnetwork control curves are obtained by sweeping the pressure head  $\Delta P_{PH}$  in the non-linear constraint (26) from 40 % to 90 % in steps of 10 % of the design case. For each case, an optimization run is performed and the optimized mass flow rate is recorded. The LMD-Control curve of the subnetwork intersects the main network characteristic curves in Point A and B. Failure 1 has larger  
500 impact than Failure 2 on the fluid-dynamic performance of the subnetwork. In this case, the system can be operated with 65.1 % of the design pressure head and 82.5 % of the design inlet mass flow rate. Point B locates at 78.3 % and 90.0 % of the design pressure head and inlet mass flow rate respectively. When the subnetwork is operated through the C-Control, fluid dynamic equilibrium  
505 moves to Point A' and B', with higher inlet mass flow rate and lower available pressure head compared to A and B.

Figure 12 shows the thermal mismatch field  $\|\Delta\Phi\|$  obtained in Points A, B, A' and B'. Note that to obtain these results four additional optimization runs have been performed in which the maximum pressure head  $\Delta P_{PH}$  has been set

510 according to the interpolated pressure head of the four points. The optimized inlet mass flow rates present negligible differences from the ones predicted through the piece-wise linear trend shown in Figure 11(b) and previously discussed. For both Failure 1 and Failure 2, the LMD-Control allows obtaining a nearly flat thermal mismatch field. In Points A and B, all the network users are equally  
515 under-heated by roughly 7 % and 4 % and discomfort peaks are avoided. Operating the network with the C-Control (Points A' and B') results in a strong thermal imbalance. Users located in the northern portion of the system are more under-heated compared to the ones located in the southern portion. This can be explained by the absence of looping branches in the northern portion,  
520 yielding higher fluid-dynamic resistance. Despite this general trend, the thermal mismatch distribution is highly oscillating and presents multiple local minima. Whether a building thermal request is satisfied depends on both the available pressure head and the nominal pressure head at each user location. The latter can vary substantially across thermal users. Table 3 summarizes the smooth  
525 maximum discomfort  $z$  obtained in the 4 points analyzed. Compared to the conventional operation strategy in use today, the LMD-Control allows reducing our global discomfort measure by roughly 62 % and 72 % in the two failure cases considered.

This study demonstrates that LMD-Control implemented at the subnetwork  
530 level can also handle failures in the transportation network. The impact of the malfunction is dampened by obtaining a homogeneous thermal mismatch field where all users are only slightly under-heated.

## 6. Conclusions

In this paper, we presented a control strategy for handling DH failures in  
535 real-time leading to minimal impact on thermal comfort of users. We minimized an original and differentiable global measure of discomfort. The optimization problem was solved using a gradient-based optimizer to allow for easy integration of feedback from distributed meter readings. Objective gradients were obtained by solving a discrete adjoint problem. This allowed computing control  
540 sensitivities with respect to the setting of a large number of valves cheaply and quickly.

Results show that our control strategy eliminates steep discomfort peaks that naturally arise when taking decentralized control actions. Local criticalities disappear at the beginning of the optimization resulting in a discomfort field  
545 with mild spatial gradients. The maximum discomfort obtained with the LMD-Control and no additional pressure head is 45 % lower than the one obtained with the C-Control and 84 % additional pressure head. This suggests that moving to a centralized operation of the system can yield considerable investment savings on pumping equipment. However, the way additional pressure head influences the  
550 optimized system performance strongly depends on the topology of the network requiring case-by-case analysis. The last study provided numerical evidence that using the LMD-Control at the distribution network level yields benefits also in case of failures in the transportation network. Compared to the conventional

operation strategy, we obtained a reduction of the maximum discomfort of 62 % and 72 % in two different failure cases considered.

This work dealt only with steady-state design conditions. Considering the complete dynamic of the system in a model predictive control tool was beyond the scope of this paper but deserves attention in future research.

## References

- [1] H. Wang, W. Yin, E. Abdollahi, R. Lahdelma, W. Jiao, Modelling and optimization of CHP based district heating system with renewable energy production and energy storage, *Applied Energy* 159 (2015) 401–421. doi:10.1016/j.apenergy.2015.09.020.
- [2] A. Franco, M. Versace, Optimum sizing and operational strategy of CHP plant for district heating based on the use of composite indicators, *Energy* 124 (2017) 258–271. doi:10.1016/j.energy.2017.02.062.
- [3] Y. Li, J. Xia, H. Fang, Y. Su, Y. Jiang, Case study on industrial surplus heat of steel plants for district heating in northern china, *Energy* 102 (2016) 397–405. doi:10.1016/j.energy.2016.02.105.
- [4] G. Schweiger, J. Rantzer, K. Ericsson, P. Lauenburg, The potential of power-to-heat in swedish district heating systems, *Energy* doi:10.1016/j.energy.2017.02.075.
- [5] H. J. Quintana, M. Kummert, Optimized control strategies for solar district heating systems, *Journal of Building Performance Simulation* 8 (2) (2014) 79–96. doi:10.1080/19401493.2013.876448.
- [6] C. Winterscheid, J.-O. Dalenbck, S. Holler, Integration of solar thermal systems in existing district heating systems, *Energy* doi:10.1016/j.energy.2017.04.159.
- [7] I. Vallios, T. Tsoutsos, G. Papadakis, Design of biomass district heating systems, *Biomass and Bioenergy* 33 (4) (2009) 659–678. doi:10.1016/j.biombioe.2008.10.009.
- [8] I. Vallios, T. Tsoutsos, G. Papadakis, An applied methodology for assessment of the sustainability of biomass district heating systems, *International Journal of Sustainable Energy* 35 (3) (2014) 267–294. doi:10.1080/14786451.2014.895005.
- [9] P. A. Østergaard, H. Lund, A renewable energy system in frederikshavn using low-temperature geothermal energy for district heating, *Applied Energy* 88 (2) (2011) 479–487. doi:10.1016/j.apenergy.2010.03.018.
- [10] N. Yamankaradeniz, Thermodynamic performance assessments of a district heating system with geothermal by using advanced exergy analysis, *Renewable Energy* 85 (2016) 965–972. doi:10.1016/j.renene.2015.07.035.

- [11] H. Lund, S. Werner, R. Wiltshire, S. Svendsen, J. E. Thorsen, F. Hvelplund, B. V. Mathiesen, 4th generation district heating (4gdh), *Energy* 68 (2014) 1–11. doi:10.1016/j.energy.2014.02.089.
- 595 [12] M. Valinčius, M. Vaišnoras, A. Kaliatka, Study and demonstration of pressure wave-based leak detection in a district heating network, *Structure and Infrastructure Engineering* (2017) 1–12doi:10.1080/15732479.2017.1330892.
- [13] E. Carpaneto, P. Lazzaroni, M. Repetto, Optimal integration of solar energy in a district heating network, *Renewable Energy* 75 (2015) 714–721. doi:10.1016/j.renene.2014.10.055.
- 600 [14] D. G. Jamieson, U. Shamir, F. Martinez, M. Franchini, Conceptual design of a generic, real-time, near-optimal control system for water-distribution networks, *Journal of Hydroinformatics* 9 (1) (2007) 3. doi:10.2166/hydro.2006.013.
- 605 [15] U. Shamir, E. Salomons, Optimal real-time operation of urban water distribution systems using reduced models, *Journal of Water Resources Planning and Management* 134 (2) (2008) 181–185. doi:10.1061/(asce)0733-9496(2008)134:2(181).
- 610 [16] E. Guelpa, C. Toro, A. Sciacovelli, R. Melli, E. Sciubba, V. Verda, Optimal operation of large district heating networks through fast fluid-dynamic simulation, *Energy* 102 (2016) 586–595. doi:10.1016/j.energy.2016.02.058.
- [17] S. Liberatore, G. M. Sechi, Location and calibration of valves in water distribution networks using a scatter-search meta-heuristic approach, *Water Resources Management* 23 (8) (2008) 1479–1495. doi:10.1007/s11269-008-9337-6.
- 615 [18] E. Creaco, G. Pezzinga, Multiobjective optimization of pipe replacements and control valve installations for leakage attenuation in water distribution networks, *Journal of Water Resources Planning and Management* 141 (3) (2015) 04014059. doi:10.1061/(asce)wr.1943-5452.0000458.
- 620 [19] C. Giacomello, Z. Kapelan, M. Nicolini, Fast hybrid optimization method for effective pump scheduling, *Journal of Water Resources Planning and Management* 139 (2) (2013) 175–183. doi:10.1061/(asce)wr.1943-5452.0000239.
- 625 [20] M. López-Ibáñez, T. D. Prasad, B. Paechter, Ant colony optimization for optimal control of pumps in water distribution networks, *Journal of Water Resources Planning and Management* 134 (4) (2008) 337–346. doi:10.1061/(asce)0733-9496(2008)134:4(337).

- 630 [21] B. Ghaddar, J. Naoum-Sawaya, A. Kishimoto, N. Taheri, B. Eck, A lagrangian decomposition approach for the pump scheduling problem in water networks, *European Journal of Operational Research* 241 (2) (2015) 490–501. doi:10.1016/j.ejor.2014.08.033.
- [22] D. F. Surco, T. P. B. Vecchi, M. A. S. S. Ravagnani, Optimization of  
635 water distribution networks using a modified particle swarm optimization algorithm, *Water Science and Technology: Water Supply* (2017) ws2017148doi:10.2166/ws.2017.148.
- [23] F. D. Paola, M. Giugni, D. Portolano, Pressure management through optimal location and setting of valves in water distribution networks using  
640 a music-inspired approach, *Water Resources Management* 31 (5) (2017) 1517–1533. doi:10.1007/s11269-017-1592-y.
- [24] H. Mala-Jetmarova, N. Sultanova, D. Savic, Lost in optimisation of water distribution systems? a literature review of system operation, *Environmental Modelling & Software* 93 (2017) 209–254. doi:10.1016/j.envsoft.  
645 2017.02.009.
- [25] A. Pizzolato, A. Sciacovelli, V. Verda, Discrete adjoint sensitivities for the real-time optimal control of large district heating networks during failure events, in: *Volume 6A: Energy*, ASME, 2016. doi:10.1115/imece2016-66734.
- 650 [26] E. Guelpa, A. Sciacovelli, V. Verda, Thermo-fluid dynamic model of large district heating networks for the analysis of primary energy savings, *Energy*doi:10.1016/j.energy.2017.07.177.
- [27] J. A. Bondy, U. S. R. Murty, *Graph theory with applications*, Vol. 290, Citeseer, 1976. doi:10.1007/978-1-349-03521-2.
- 655 [28] J. H. Ferziger, M. Perić, *Computational Methods for Fluid Dynamics*, Springer Berlin Heidelberg, 1996. doi:10.1007/978-3-642-97651-3.
- [29] A. Verbart, M. Langelaar, F. van Keulen, A unified aggregation and relaxation approach for stress-constrained topology optimization, *Structural and Multidisciplinary Optimization* 55 (2) (2016) 663–679. doi:  
660 10.1007/s00158-016-1524-0.
- [30] S. Patankar, D. Spalding, A calculation procedure for heat, mass and momentum transfer in three-dimensional parabolic flows, *International Journal of Heat and Mass Transfer* 15 (10) (1972) 1787–1806. doi:10.1016/0017-9310(72)90054-3.
- 665 [31] K. Svanberg, The method of moving asymptotes—a new method for structural optimization, *International Journal for Numerical Methods in Engineering* 24 (2) (1987) 359–373. doi:10.1002/nme.1620240207.

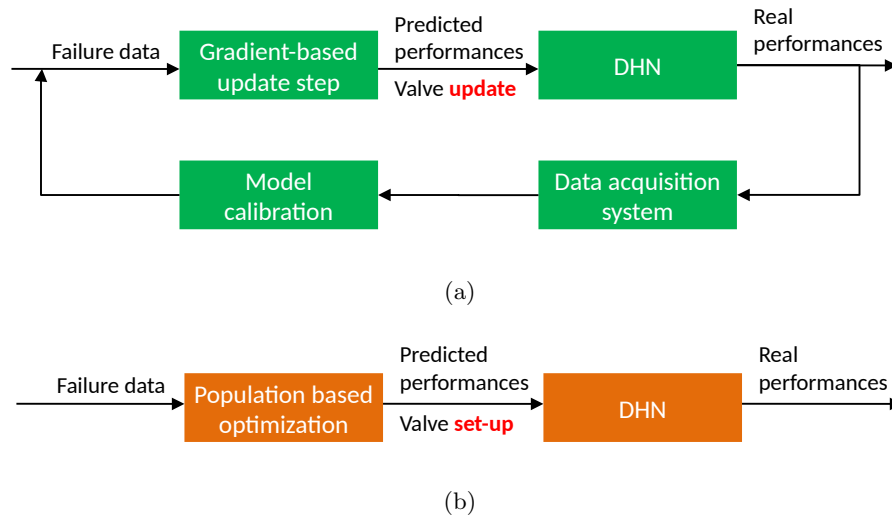


Figure 1: Control system block diagram. (a): On-the-fly feedback control with gradient-based optimizer. (b): Feed-forward control with population-based optimizer

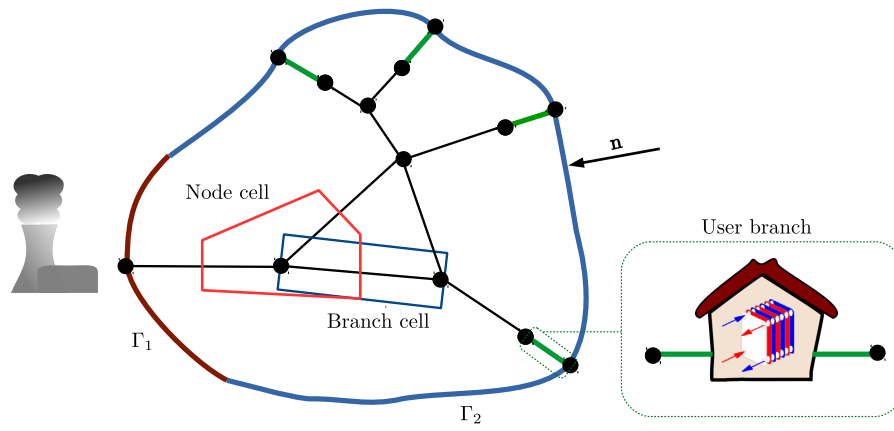


Figure 2: Schematic of the 1D model of the network



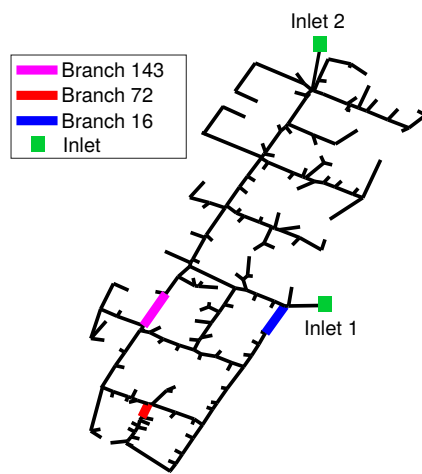


Figure 3: Distribution network overview

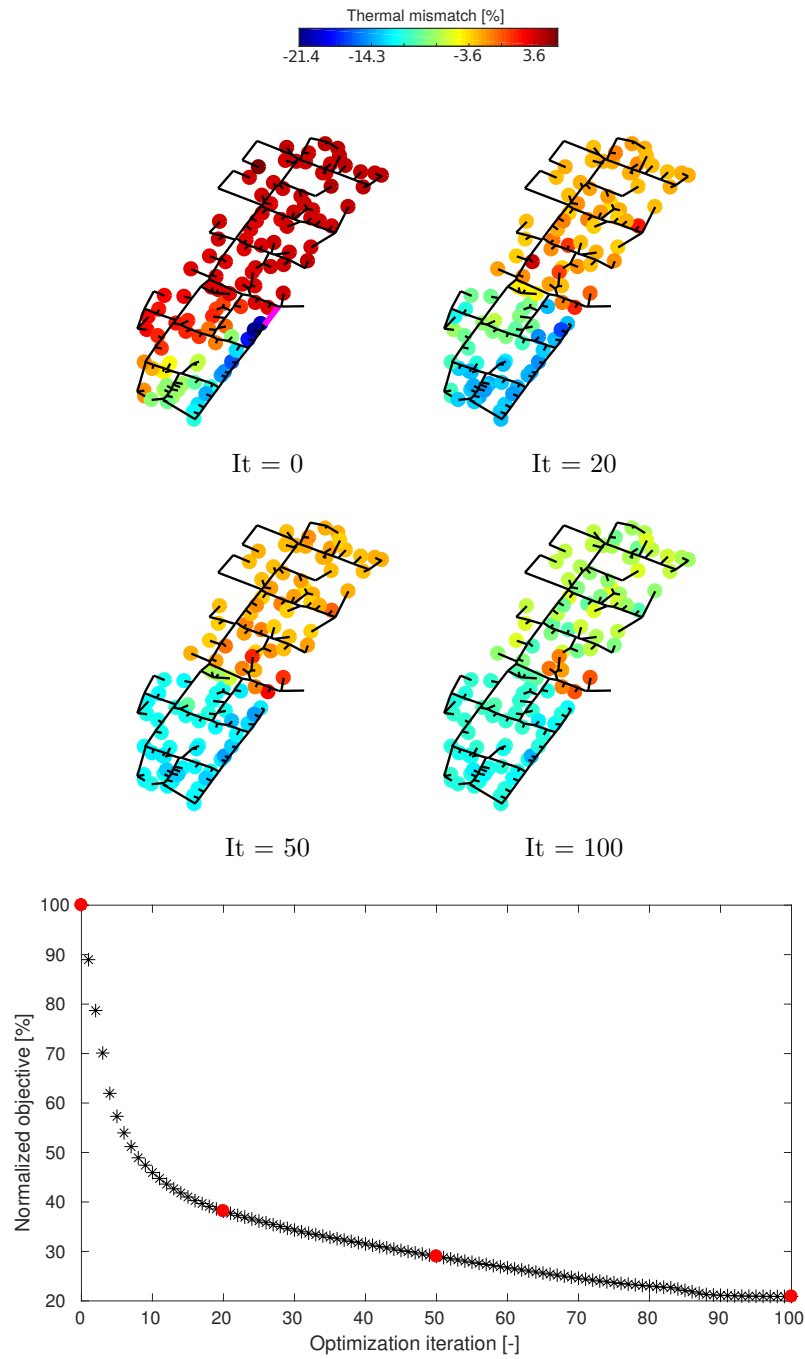


Figure 4: Objective history during the optimization with no additional pressure head. The thermal mismatch distribution in the network is shown at selected optimization iterations.

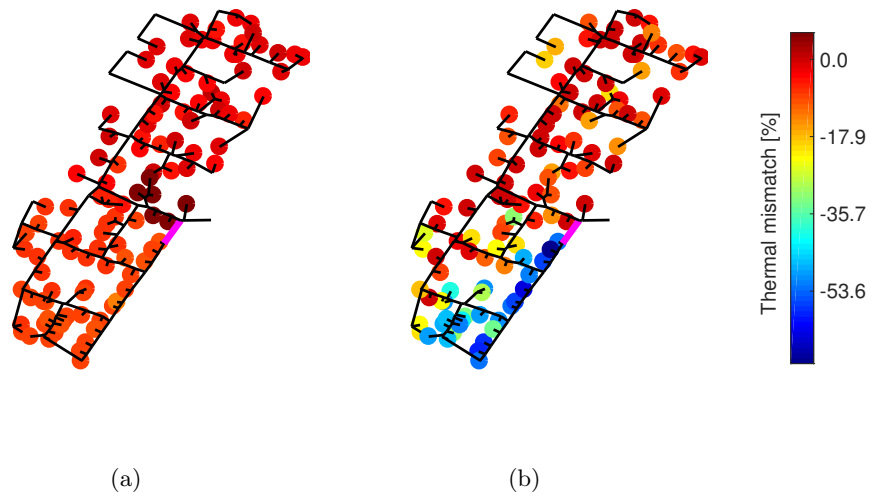
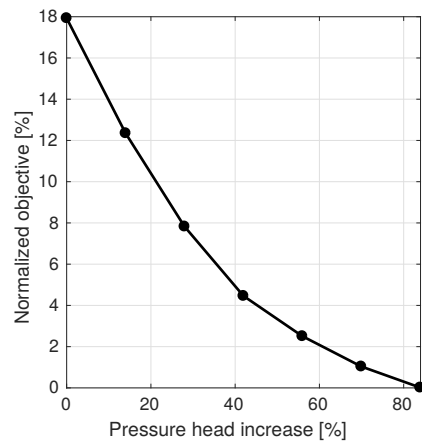
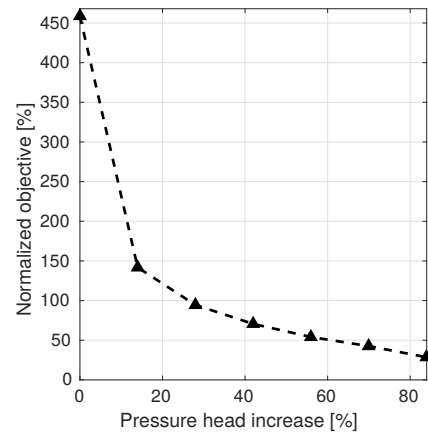


Figure 5: Final thermal mismatch field  $\|\Delta\Phi\|$  when using the LMD-Control (a) and the C-Control (b)



(a)



(b)

Figure 6: Effect of available pressure head. (a): Least Maximum Discomfort control. (b): Conventional control

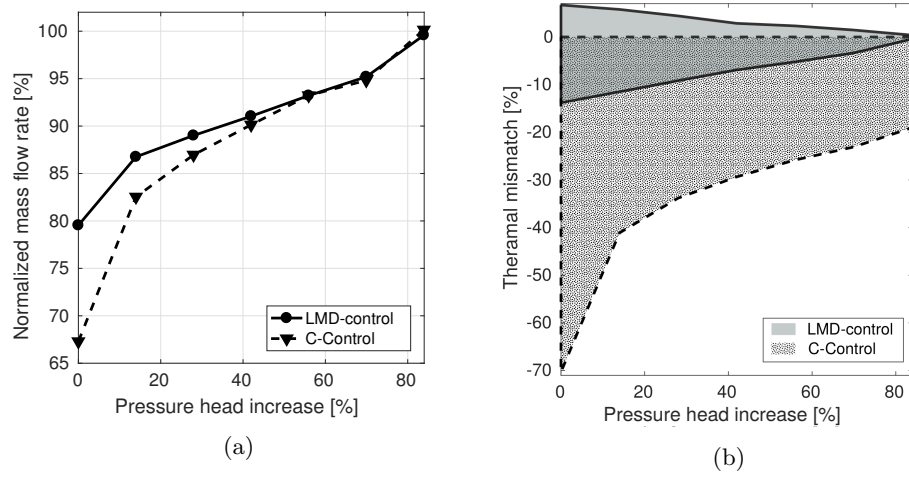


Figure 7: (a): Optimized values of the normalized mass flow rate for the LMD-Control and the C-Control . (b): Power mismatch range registered with the LMD-control and the C-Control

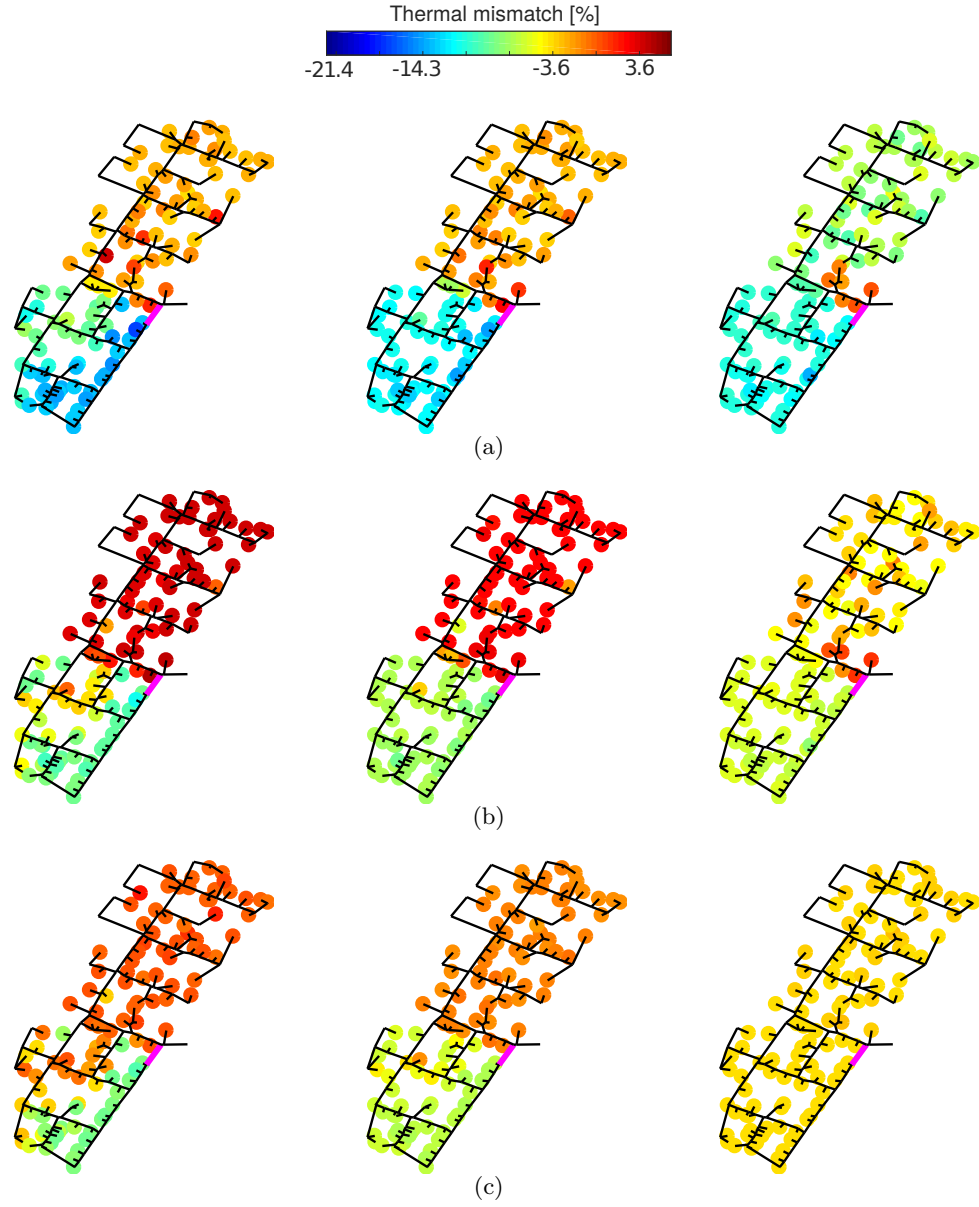


Figure 8: Evolution of the thermal mismatch distribution for  $\Delta P_{PH} = 0\%$  (a),  $\Delta P_{PH} = 42\%$  (b),  $\Delta P_{PH} = 84\%$  (c). The snapshots are taken at  $It = 20$ ,  $It = 50$ ,  $It = 100$ .

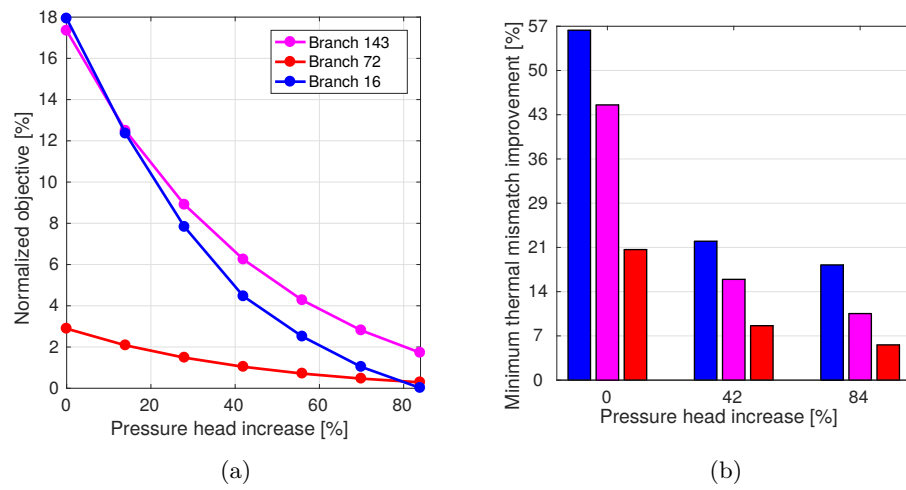


Figure 9: (a): Comparison of inlet pressure head effect with different failure locations. (b): Summary of the minimum thermal mismatch improvements achievable with the LMD-Control compared to the C-Control for different failure locations

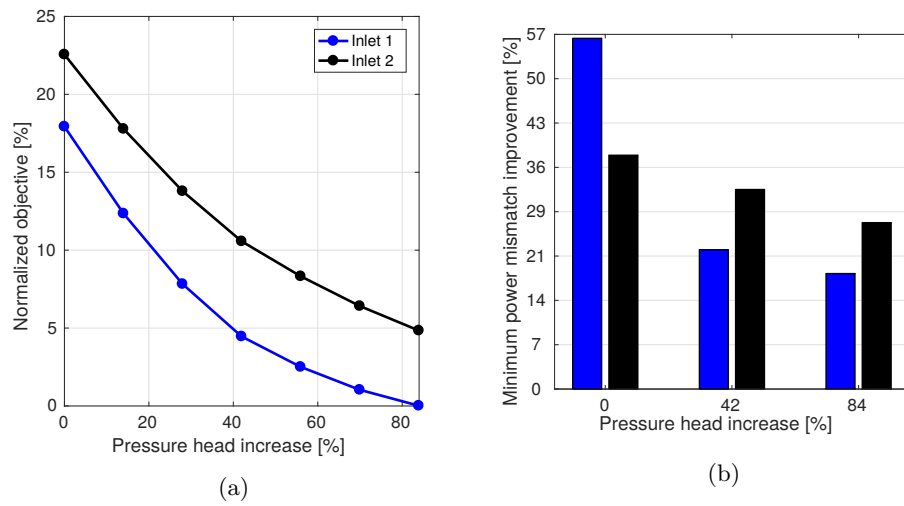


Figure 10: (a): Comparison of inlet pressure head effect with different failure locations. (b): Summary of the minimum thermal mismatch improvements achievable with the LMD-Control compared to the C-Control for different inlet locations



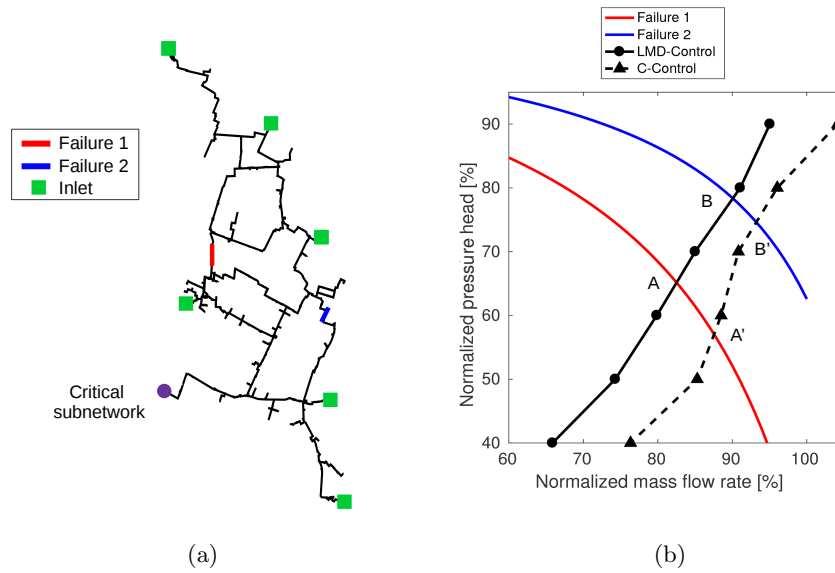


Figure 11: (a): Transportation network overview. (b): Intersection of the main network characteristic curves with the subnetwork control curves for the two failures considered

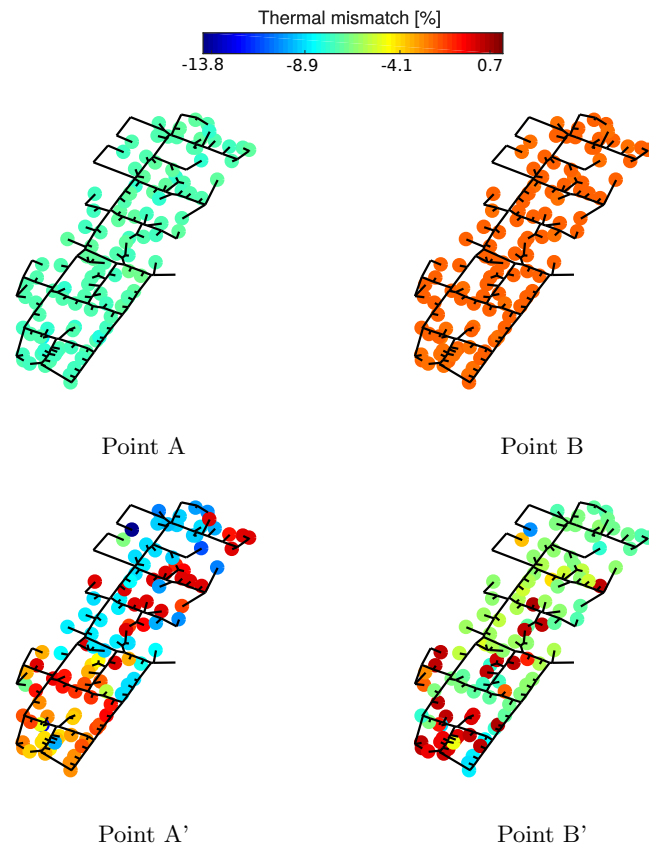


Figure 12: Final thermal mismatch field  $||\Delta\Phi||$  for failures in the main network

Table 1: MMA parameters utilized

Minimum asymptote adaptivity	0.7
Initial asymptote adaptivity	0.5
Maximum adaptivity	1.2
Constraint penalty	10000

Table 2: Model parameters and properties

Fanning friction factor	$f$ $[-]$	0.014
Water inlet temperature	$T_{in}$ $[K]$	363.15
Relative outlet total pressure	$P_{out}$ $[Pa]$	0
Water density	$\rho$ $[\frac{kg}{m^3}]$	1000
Water specific heat	$c_p$ $[\frac{J}{kg \cdot K}]$	4186
Volumetric heat transfer coefficient	$K$ $[\frac{W}{m^3 \cdot K}]$	0.9
Set-point internal temperature	$T_{sp}$ $[K]$	293.15
External temperature	$T_{ext}$ $[K]$	265.15
Minimum Local pressure drop coefficient	$\beta_{min}$ $[-]$	0
Maximum Local pressure drop coefficient	$\beta_{max}$ $[-]$	1e7
Minimum relative inlet mass flow rate	$\chi_{min}$ $[-]$	0.5
Maximum relative inlet mass flow rate	$\chi_{max}$ $[-]$	1.5

Table 3: Smooth maximum discomfort  $z$  ( $\times 10^2$ ) obtained for failures in the main network

	LMD-Control [-]	C-Control [-]
Failure 1	0.49	1.28
Failure 2	0.16	0.57